

PAPER • OPEN ACCESS

Simultaneous decoding of cardiovascular and respiratory functional changes from pig intraneural vagus nerve signals

To cite this article: Fabio Vallone *et al* 2021 *J. Neural Eng.* **18** 0460a2

View the [article online](#) for updates and enhancements.



PAPER

OPEN ACCESS

Simultaneous decoding of cardiovascular and respiratory functional changes from pig intraneural vagus nerve signals

RECEIVED
29 June 2020REVISED
5 June 2021ACCEPTED FOR PUBLICATION
21 June 2021PUBLISHED
7 July 2021Original content from
this work may be used
under the terms of the
[Creative Commons
Attribution 4.0 licence](#).Any further distribution
of this work must
maintain attribution to
the author(s) and the title
of the work, journal
citation and DOI.Fabio Vallone^{1,6} , Matteo Maria Ottaviani^{1,2,6} , Francesca Dedola¹, Annarita Cutrone¹, Simone Romeni³, Adele Macri Panarese¹, Fabio Bernini², Marina Cracchiolo¹, Ivo Strauss¹ , Khatia Gabisonia^{2,4}, Nikoloz Gorgodze^{2,4}, Alberto Mazzoni¹ , Fabio A Recchia^{2,4,5,*} and Silvestro Micera^{1,3,*}¹ The BioRobotics Institute and Department of Excellence in Robotics and Artificial Intelligence, Scuola Superiore Sant'Anna, Pisa, Italy² Institute of Life Sciences, Scuola Superiore Sant'Anna, Pisa, Italy³ Bertarelli Foundation Chair in Translational Neural Engineering, Center for Neuroprosthetics and Institute of Bioengineering, Ecole Polytechnique Federale de Lausanne, Lausanne, Switzerland⁴ Fondazione Toscana Gabriele Monasterio, Pisa, Italy⁵ Department of Physiology, Cardiovascular Research Center, Lewis Katz School of Medicine at Temple University, Philadelphia, PA, United States of America⁶ Equal contribution.

* Authors to whom any correspondence should be addressed.

E-mail: fabio.recchia@santannapisa.it and silvestro.micera@santannapisa.it**Keywords:** bioelectronic medicine, neuroprosthetics, vagus nerve, intraneural electrodes, decoding algorithm, hybrid modeling frameworkSupplementary material for this article is available [online](#)**Abstract**

Objective. Bioelectronic medicine is opening new perspectives for the treatment of some major chronic diseases through the physical modulation of autonomic nervous system activity. Being the main peripheral route for electrical signals between central nervous system and visceral organs, the vagus nerve (VN) is one of the most promising targets. Closed-loop VN stimulation (VNS) would be crucial to increase effectiveness of this approach. Therefore, the extrapolation of useful physiological information from VN electrical activity would represent an invaluable source for single-target applications. Here, we present an advanced decoding algorithm novel to VN studies and properly detecting different functional changes from VN signals. **Approach.** VN signals were recorded using intraneural electrodes in anaesthetized pigs during cardiovascular and respiratory challenges mimicking increases in arterial blood pressure, tidal volume and respiratory rate. We developed a decoding algorithm that combines discrete wavelet transformation, principal component analysis, and ensemble learning made of classification trees. **Main results.** The new decoding algorithm robustly achieved high accuracy levels in identifying different functional changes and discriminating among them. Interestingly our findings suggest that electrodes positioning plays an important role on decoding performances. We also introduced a new index for the characterization of recording and decoding performance of neural interfaces. Finally, by combining an anatomically validated hybrid neural model and discrimination analysis, we provided new evidence suggesting a functional topographical organization of VN fascicles. **Significance.** This study represents an important step towards the comprehension of VN signaling, paving the way for the development of effective closed-loop VNS systems.

1. Introduction

The autonomic nervous system (ANS) plays a crucial role in the self-governed maintenance of body homeostasis. In ANS peripheral nerves, afferent and efferent fibers run together, providing bidirectional communication between specific circuits of

the central nervous system and visceral organs. The artificial modulation of this complex circuitry is the challenging goal of bioelectronic medicine (BM), a highly promising alternative to some limited pharmacological treatments [1–4]. Among the main ANS nerves, the vagus nerve (VN) represents a privileged target as it modulates vital functions like respiration,

circulation and the digestion [5]. VN stimulation (VNS) of cervical segments has shown a great potential for the treatment of a wide range of pathological conditions such as epilepsy [6], chronic heart failure [7], and inflammatory diseases [8, 9]. However, the formidable amount of afferent and efferent signals that simultaneously cross this VN segment, the VNS side-effects [10] and the discovery of VN involvement in the regulation of complex functions like immunity [11] or central neuroplasticity [12, 13] highlight the need for high precision and selectivity. In an ideal scenario, the therapeutic stimulation or inhibition of VN or any other ANS nerve should be: (a) selectively directed to specific efferent or afferent fibers and (b) regulated by a closed-loop control, thus adapting the stimulation to the evolving conditions of the patients [14–17]. Importantly, the co-existence of afferent and efferent signals in the VN points to the possibility that the feedback loop is originated and closed at the same anatomical site. Nonetheless, VNS applications are realized using epineural cuff-like electrodes, because of their relatively low invasiveness and versatility for chronic implants [18–21].

Different strategies have been recently adopted to extract function-specific markers from neural activity using epineural electrodes [4, 22–26]. Specific neurograms related to the respiratory cycle [22, 23] and blood pressure fluctuations [4] were recorded from pig VN using bipolar/tripolar ring cuff electrodes, while decoding strategies and methodological frameworks led to the identification of cytokine- and hypoglycemia/hyperglycemia-specific neural activity markers in murine VN and carotid sinus nerve [24–26]. However, epineural electrodes often display a limited selectivity and can only record the compound activity that provides a global picture of neural signal trafficking [27–29]. Therefore, intraneural electrodes have been developed and successfully employed to enhance selectivity and increase the signal-to-noise ratio of recordings [30, 31] in somatic nerves [14, 17, 31, 32]. Nevertheless, this technology has received very limited attention for VN applications. To date, intraneural recordings in VNs have been obtained in humans [33], using an ultrasound-guided microneurography approach that is very convenient for minimally invasive signal acquisition, but not for closed-loop stimulations, and in pigs [34], in which neural activity was assessed only at the steady state with limited signal recording capacity (i.e. four-channel electrode longitudinally implanted).

Here, we performed the first comprehensive study testing intraneural VN recording for the identification of specific signals elicited by changes in physiological parameters. To this aim, we recorded VN activity through intraneural multi-channel electrodes in anaesthetized pigs at baseline and during alterations in blood pressure and respiratory parameters, collectively named ‘functional challenges’. Different from rodents, but similar to humans, axons of porcine

VN are clustered to form multiple fascicles [35]. Therefore, to discriminate between nerve activity at baseline and during functional challenges and to investigate a possible functional organization of VN fascicles, we developed novel decoding algorithms and hybrid modeling framework.

2. Materials and methods

2.1. Animals

This study was conducted in six castrated male farm pigs (*Sus Scrofa Domestica*) 3–4 month old and weighing 30–40 kg. The animals were housed in the vivarium at controlled room temperature (24 °C) and fasted overnight before anesthesia with free access to water. All animal handling and experimental procedures were performed according to European Community guidelines (EC Council Directive 2010/63). The animal protocol was approved by the Italian Ministry of Health and was in accordance with the Italian law (D.lgs. 26/2014).

2.2. Anesthesia and monitoring of physiological parameters

On the day of the experiment, pigs were anesthetized and prepared for surgery as previously described by us [36]. They were sedated with a cocktail of 4 mg kg⁻¹ tiletamine hydrochloride and 4 mg kg⁻¹ zolazepam hydrochloride injected intramuscularly, intubated and mechanically ventilated. The respiratory frequency was fixed to ten respiratory cycles per minute and the tidal volume (TV) to 10 ml kg⁻¹. The combination of these respiratory parameters resulted in PaO₂ > 100 mmHg, PaCO₂ < 40 mmHg and arterial blood pH in the range of 7.4–7.45. Arterial blood gases analysis was repeated at least every 30 min. A pulse oximeter was applied on the tongue to continuously monitor arterial oxygen saturation, which was stably above 96% for the duration of the experiment. Inhalatory anesthesia was maintained with a mixture of 1%–1.5% isoflurane dissolved in 79% air and 21% oxygen. The respiratory pressure was recorded by connecting the airflow of the ventilator to a pressure transducer. Electrocardiogram (ECG) and arterial systolic, diastolic and mean blood pressure were constantly monitored and recorded. ECG was recorded using Ag–AgCl surface electrodes and aortic blood pressure was recorded using a solid-state pressure transducer catheter (Millar, SPR-100) inserted in the left femoral artery with the tip positioned in the abdominal aorta. This catheter was also used to withdraw arterial blood for blood gas analysis. Respiratory pressure, ECG and aortic blood pressure signals were sampled at 24 414 Hz, amplified, digitized and low-pass filtered with downsampling (Butterworth fourth-order) at 10 Hz, 50 Hz, 25 Hz, respectively (RZ5D BioAmp Processor, Pz5, Tucker-Davis Technologies Inc., TDT, USA).

Glycemia was checked every 30 min and before each recording session to assess the stability of plasma glucose levels above 100 mg/100 ml. The main ear vein was cannulated for the intravenous administration of all the drugs.

2.3. Surgical preparation and electrode implantations

The six pigs were named p1, p2, p3, p4, p5 and p6. To isolate the cervical VN, a midline cervical incision was made along a segment comprised between the larynx and the sternum, as previously described by us [37]. After identifying the neurovascular bundle of the neck (common carotid artery, internal jugular vein and VN), the left ($n = 3$, p1, p2 and p3) and right ($n = 3$, p4, p5 and p6) cervical VNs were carefully separated from the common carotid artery by blunt dissection, 3–4 cm above and below the cricoid cartilage. The sympathetic trunk, attached dorsally to the VN, was gently detached and pulled apart. In all animals, electrodes were implanted in the cervical VN at the level of the cricoid cartilage, which was used as an anatomical reference to standardize implant positioning across animals. In p1 and p2, the left VN was implanted with a transverse intrafascicular multichannel electrode (TIME) [38] endowed with ten active sites (p1–t1 and p2–t2), following the same procedures described by Badia *et al* [39]. Similarly, the right VN of p5 and p6 was implanted with two TIMEs each, endowed with 16 active sites, spaced 3–4 cm apart (p5–t3;p5–t4; p6–t5;p6–t6). In p3 and p4, the left and right VNs, respectively, were implanted with two self-opening intraneural peripheral interfaces (SELINES) endowed with 13 (p3–s1,p3–s2) and 7–13 (p4–s3, p4–s4) active sites, respectively, as described by Cutrone *et al* [40]. All the intraneural electrodes were inserted obliquely, forming a 45° angle with the longitudinal axis of the nerve, except for two SELINES, one in p3 and one in p4, that were inserted along the transverse axis. In all the experiments, the ground electrode was inserted under the skin of the left elbow of the animal. See also (supplementary table 1 (available online at stacks.iop.org/JNE/18/0460a2/mmedia)) for a summary description of electrode type and VN side in each pig.

2.4. Tissue isolation and histology

At the end of the experiment, the anesthetized pigs were euthanized by an intravenous injection of saturated KCl solution. Intraneural electrodes were left in place and the VN was cut 3 cm above and below the insertion site and gently placed on a dedicated support to avoid twisting. The VN samples were then fixed in 4% paraformaldehyde for 18–20 h, rinsed in PBS, dehydrated in a series of progressively more concentrated solutions of ethanol/xylol and finally embedded in paraffin wax. Transverse sections (10 μm thick) were cut, deparaffinized, rehydrated,

processed for routine hematoxylin and eosin and mounted in silane-coated slides. Images were captured with 5 \times magnification by a Leica DMRB microscope equipped with the DFC480 digital camera (Leica Microsystems, Cambridge, UK). Sections at the level of the implanted electrodes were aligned and manually segmented to study the electrode–nerve interaction. The nerve was cross-sectioned for the entire length of the implants, with the two SELINES fixed in site, and stained with hematoxylin and eosin. Light microscopy observations of VN sections showed the fascicular structure of the nerve and holes caused by the electrode insertion, with SELINE polyimide strips preserved in a few slices. No macroscopic and microscopic signs of hemorrhages were found.

2.5. In vivo recording of VN activity

Neural recordings started at least 30 min after electrode implantation to allow for stabilization of the nerve and of physiological parameters. The neural signals were first acquired over 5 min at baseline, followed by recording sessions in which physiological parameters were altered (functional challenges). The baseline condition was defined as the time when mean aortic blood pressure (mean aortic BP) and heart rate were found stable for at least 30 min after completion of electrodes implantation. We empirically considered these parameters stable if their variations were less than 5% across 5 min consecutive intervals.

At baseline, RR and TV were fixed at ten respiratory cycles per minute and 10 ml Kg^{-1} , respectively. The functional challenges (C) consisted of (a) BPC, i.e. increase in mean aortic BP up to 150% of the baseline value obtained with an intravenous infusion of 80 ng $\text{kg}^{-1} \text{min}^{-1}$ of Ang II (Sigma Aldrich), a vasopressor with rapidly reversible effects [41] (b) TVC, i.e. increase in TV to 125% of baseline value in p2, p5, p6 and 200% ml in p3 and p4 for 2 min and (c) RRC, i.e. increase in RR from 10 to 15 respiratory cycles/min in p2,p5, p6 and 20 respiratory cycles/min in p3 and p4 for 2 min. We limited TV increase to 125% and RR increase from 10 to 15 respiratory cycles/min in p2, p5 and p6 because larger increases caused significant (>5%) fluctuations of systolic and diastolic BP values.

To obtain the desired vasopressor effect, AngII infusion was maintained for 8.9 ± 1 min ($n = 6$) and mean aortic BP increased from 78 ± 4.3 mm Hg up to 114 ± 6.6 mmHg ($n = 6$). (see also supplementary table 1 for a summary description of type of challenges in each pig).

These challenges were produced in random order and each one was followed by a recovery period of at least 5 min to let the physiological parameters return to baseline values. These functional challenges and the consequent changes in physiological parameters were in the same range of the ones used and proved suitable for neural VN recordings in anesthetized pigs by Sevcencu *et al* [22]. Glycemia and blood gases

were checked before and after the completion of each functional challenge.

2.6. Data acquisition and decoding algorithm

VN raw multichannel signals were acquired at a frequency sampling of 24.4 kHz, high pass filtered at 5 Hz and digitally amplified (RZ5D BioAmp Processor, Pz5, Tucker-Davis Technologies Inc., TDT, USA). Each channel of the raw recordings was segmented by using a 1 s temporal window and rescaled to zero mean and unitary standard deviation. Discrete wavelet transform [42, 43], at a maximum level equal to 4, was applied on the segmented portions of each channel by using a symlet 7 wavelet function [14, 44]. Approximation coefficients relative to frequencies $\lesssim 1500$ Hz were discarded in the subsequent analysis. Principal component analysis on the multivariate wavelet details was applied independently at two different scales [45] relative to frequency ranges of $\cong 1500$ –3000 Hz and 3000–6000 Hz, respectively. The first three principal components (explaining the majority of the variance of the dataset, i.e. >70%) were retained to build a feature vector for the classification algorithm. For testing purposes, in each pig we divided the dataset into $K_{\text{test}} = 3$ cross-validation folds at random. We, thus, calculated the mean accuracy over the three different test sets to rule out concerns on particular test set randomly selected.

Ensemble of classifiers was created by using a boosting algorithm [46, 47]. In particular, the random undersampling boosting (RUSBoost) technique was considered to deal with class imbalance problem [47, 48] (see supplementary table 1 for a summary of the number of observation of each challenge in each pig). The classifiers that are used in the ensemble were trees [46, 47]. To optimize the hyperparameters present in our ensemble, we applied a cross validation scheme with $K_{\text{opt}} = 5$ fold (this was done in each one of three different train data portions previously selected by the cross-validation scheme with $K_{\text{test}} = 3$).

We optimized the maximum depth, number of cycles (number of trees) and learning rates via grid search by considering the minimum of the cross-validated misclassification rate as a function of the above hyperparameters.

Specifically, we tested four different values of learning rates (i.e. [0.1, 0.25, 0.5, 1]) and for each one we varied the maximal depth as a power of 3^m with m chosen such that 3^m was no greater than $n-1$, where n was the number of elements in the train set. We then plotted, for each learning rate and for each maximal depth, the cross-validated misclassification rate as a function of the number of trees (number of cycles) ranging from 1 to 500. Finally, we considered as optimal hyperparameters those that yielded the minimal cross-validated misclassification rate. Data were analyzed off-line in MATLAB (The MathWorks, Inc.). In figure 1, a summary of the experimental setup and decoding algorithm procedure is shown.

2.7. Discrimination analysis and decoding-discrimination relationship

Similarly to previous studies [49], we built a discrimination channel index to assess the discrimination ability of the electrodes and thus a possible relation with decoding performances. To this aim, we calculated the percentage of activation for each channel relative to the different functional challenges as described below.

For each challenge, each signal was reconstructed using the wavelet details at the same scale previously used for the decoding algorithm:

$$x_s(t) \approx \sum_{j=1}^2 \sum_k d_{s,j}[k] * \psi_{jk}(t)$$

where $d_{s,j}[k]$ are the wavelet details at scale j of the recording site s , and $\psi_{jk}(t)$ is the wavelet function (see supplementary figures 3(a) and (b) for a graphical example). The reconstructed signals from each recording sites ($X = \{x_s\}, i = 1, \dots, S$) were segmented using a temporal window of $T = 1$ s and rescaled to zero mean and unitary standard deviation obtaining a number of signal's blocks N_{block} , i.e. $X = (X(1), \dots, X(N_{\text{block}}))$. For each block of the signals, we calculated the first three principal component coefficients (loadings), i.e. $P^{i_{\text{pca}}}(i_{\text{block}})$ with $i_{\text{pca}} = 1, 2, 3$ and $i_{\text{block}} = 1, \dots, N_{\text{block}}$. We thus identified for each principal component the higher outliers relative to loadings' absolute values. Outliers were identified using a threshold of three scaled mean absolute deviation from the median (see supplementary figure 3(c)), right panel for a graphical example). When an outlier was identified in a portion of the signal, a value equal to unity was assigned to the corresponding channel ('channel activated') and zero otherwise, i.e. we defined an indicator for each channel s and block i_{block} :

$$I_s^{i_{\text{pca}}}(i_{\text{block}}) = \begin{cases} 1 & \text{if loading of } i_{\text{pca}} \text{ w.r.t. channels is outlier} \\ 0 & \text{otherwise} \end{cases}$$

For each channel, the resulting percentage of activation relative to a principal component $\mu_s^{i_{\text{pca}}}$, is equal to the number of times in which the channel was activated divided by the total number of portions of the signal, i.e.

$$\mu_s^{i_{\text{pca}}} = \frac{\sum_{i_{\text{block}}=1}^{N_{\text{block}}} I_s^{i_{\text{pca}}}(i_{\text{block}})}{N_{\text{block}}}$$

The percentage of activation of each channel was quantified as the mean over the percentage of activation of the channel in each principal component (see supplementary figure 3(c) left panel) $\mu_s = \frac{\sum_{i_{\text{pca}}=1}^3 \mu_s^{i_{\text{pca}}}}{3}$.

Similarly to Raspopovic *et al* [49], given the percentage of activation for each channel, we defined a discrimination index for each channel as the

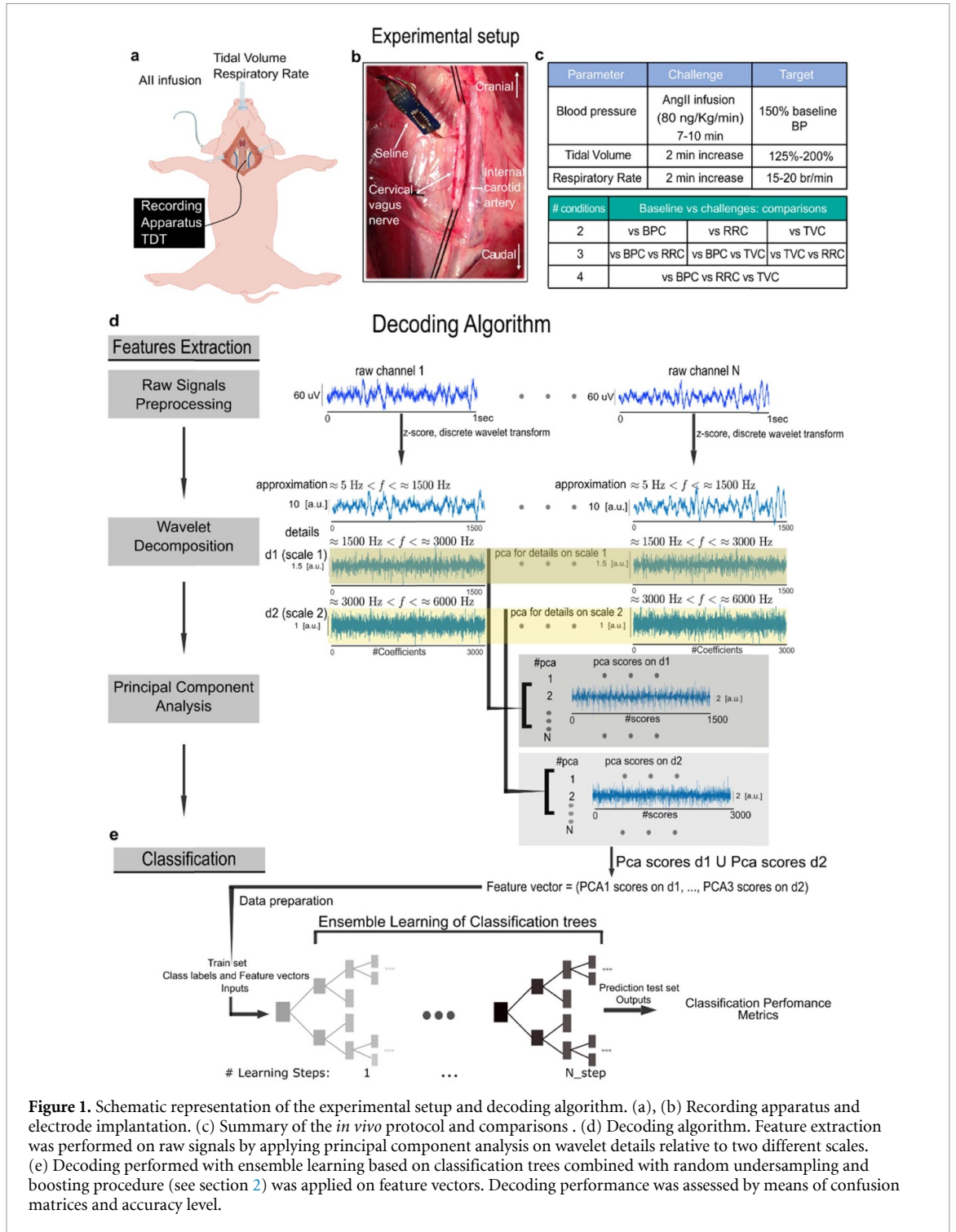


Figure 1. Schematic representation of the experimental setup and decoding algorithm. (a), (b) Recording apparatus and electrode implantation. (c) Summary of the *in vivo* protocol and comparisons. (d) Decoding algorithm. Feature extraction was performed on raw signals by applying principal component analysis on wavelet details relative to two different scales. (e) Decoding performed with ensemble learning based on classification trees combined with random undersampling and boosting procedure (see section 2) was applied on feature vectors. Decoding performance was assessed by means of confusion matrices and accuracy level.

difference between the percentage of activation of the considered channel and the mean percentage of activation over the remaining channels, i.e.

$$D_s = \mu_s - \frac{1}{N_s - 1} \sum_{s=1, i \neq l}^{s=1, i \neq l} \mu_l.$$

Thus, discrimination vectors with entries made of channels' discrimination indices were obtained among the different functional challenges, i.e. $D_c = \{D_{c,s}\}$ with $c = \{\text{Baseline, BPC, TVC, RRC}\}$ and $s = 1, \dots, S$. The difference between two generic

discrimination vectors was obtained by considering the root mean square level of the Euclidean distance (see supplementary figure 4(a)).

Electrode discrimination ability was computed by considering the mean over all the six possible combination distances between the distinct discrimination vectors (see supplementary figure 4(a)). Finally, to assess linear correlations between accuracy (Acc) and electrode discrimination ability (EDA) we employed a linear mixed model treating the different animals (Animal) as a random effect, i.e. $\text{Acc} \sim \text{EDA} + (1|\text{Animal})$.

2.8. Hybrid modeling of the recording process and Discriminative Field Potentials (DFPs)

To understand the distribution of the electrical field potential within a nerve, we employed the hybrid modeling framework previously described by us [49–51]. Histological sections were manually segmented by defining the contours of the epineural compartment (the whole nerve section contour) and of the fascicles. Such contours were imported in MATLAB as closed polylines. Fascicle polylines were substituted with ellipses having the same surface area as the fascicles; center of the fascicle centroid, axis length ratio and orientation were deduced from the minimum (area) bounding rectangle of each fascicle. The perineurial sheath for each fascicle was defined as a layer with width equal to 0.03 times the effective diameter (diameter of the equivalent circle) of the fascicle [52]. A 3D extrusion of the given nerve section was defined in COMSOL (through MATLAB LiveLink for COMSOL) and was included in a saline bath the external surface of which was grounded (simulation of zero potential at infinity [50]). A point current source was defined corresponding to each electrode active site center. To obtain the potential field on the nerve section (up to a multiplicative scaling factor, i.e. linearity assumption), we simulated the stimulation from all given sites with an adimensional current (one at the time and unitary). In fact, thanks to the Helmholtz reciprocity theorem, the value of the potential field due to a unitary current injected by an active site corresponds to the impedance that relates the intensity of a current source with the resulting potential field recorded at the site surface. This means that a higher electrical field in a point in space P leads to a higher amplitude of the recorded electrical activity of a fiber located in P [53]. Given the knowledge of the electric field potential generated from a fascicle and the corresponding recording capability of a given recording site, we wanted to link this information to the discrimination properties of the recording site. To this aim, we defined a measure, that we called DFP, by weighting the recording capabilities of a recording site s from a given fascicles F together with the discrimination properties of the recording site s related to a functional challenge c , i.e.

$$DFP_{c,F} = \frac{\sum_{s=1}^S D_{c,s} \varphi_{s,F}}{\sum_{s=1}^S \varphi_{s,F}}$$

where $D_{c,s}$ is the discrimination ability to a functional challenge c and recording site s , and $\varphi_{s,F}$ is the mean field inside a fascicle F recorded from a site s (calculated by averaging isopotential values of the potential field inside the fascicle). Since the $\varphi_{s,F}$ measures how a site s is capable of recording from a given fascicle, and $D_{c,s}$ measures how site s records better the activity related to a functional challenge c with respect to the other sites, then the $DFP_{c,F}$ is a quantity measuring

how a fascicle is related to a given functional challenge. Similarly to the calculation of electrode discrimination ability, to quantify the discrimination ability of the whole nerve section, we computed the root mean square level of the Euclidean distance of the DFP values in the fascicle space. We thus calculated the mean discrimination distance by considering the mean over all the six possible combinations of functional challenges.

2.9. Statistical analysis

Unless otherwise stated, data are expressed as mean \pm s.e.m. Statistical significance between accuracies within the same animal were assessed by means of Chi square test followed by Bonferroni correction for multiple comparisons. Confidence intervals for the accuracy values were calculated using the Clopper–Pearson method. Statistical significance of accuracy values with respect to chance level was assessed by using the binomial test. Statistical significances across animals were assessed by a two-way ANOVA, followed by Tukey–Kramer test for multiple comparisons, considering as the VN side (left or right) and electrode type (TIME or SELINE) as the two categorical variables. Normality of the residuals was assessed with a Lilliefors test, setting the significance threshold to $p = 0.05$. Statistical significance between the discrimination ability of nerve sections was assessed by using two-tailed paired t -test at a significance threshold of 0.05. To test for normality of data distribution, a Kolmogorov–Smirnov test was used for each dataset. To check the statistical significance of the correlations between accuracy and EDA, we employed an F-test with F distribution having degrees of freedom ($df_1 = 1$, $df_2 = 22$). All the statistical analyses were performed with MATLAB (The MathWorks, Inc.).

3. Results

3.1. Decoding tasks to classify functional challenges against baseline

We tested our decoding algorithm in different scenarios, i.e. by considering in our dataset a progressively larger number and type of functional challenges, respiratory (TVC and RRC) and cardiovascular (BPC). In four pigs (p3, p4, p5 and p6) we also studied the variation of the decoding performances, in a single animal and for the same nerve, relative to the different positioning of two pairs of SELINEs (s1, s2; or s3, s4) and two pairs of TIME (t3, t4; or t5,t6). We thus tested the following combinations: p3–s1 vs. p3–s2; p4–s3 vs. p4–s4; p5–t3 vs. p5–t4 and p6–t5 vs. p6–t6 (see section 2.9 for details on the statistical analysis). Moreover, we also compared the animals for possible effects of the electrode type and VN side on mean decoding performances (see also supplementary figure 1).

3.2. Decoding the response to a single functional challenge

We started with the simplest case in which we sought to discriminate only one of the three functional challenges against baseline. For baseline vs BPC, we achieved a mean high accuracy level over the different recordings equal to $82.9 \pm 5.8\%$, as shown in figure 2(a) ($n = 9$, see supplementary figure 2(a) for confusion matrices). A dependence on electrode position within the same nerve was observed in pigs p4 and p6. Indeed, the accuracy value for p4–s3 (95.5%, [93.8%, 96.7%] confidence interval $p = 0.05$, figure 2(a)) was greater than p4–s4 (71%, [67.7%, 74.2%] Confidence Interval $p = 0.05$, figure 2(a)) ($p < 0.001$ Chi square test, Bonferroni correction). Moreover, in pig p6 implanted with TIME t5 and t6, i.e. p6–t5 and p6–t6, we achieved a lower level of accuracy for p6–t5 (81%, [78.3%, 83.5%] confidence interval $p = 0.05$, figure 2(b)) with respect to p6–t6 (95.4%, [93.8%, 96.7%] confidence interval $p = 0.05$, figure 2(b)) ($p < 0.001$ Chi square test, Bonferroni correction).

Only in one animal (p5–t3 and p5–t4) the accuracies were low with p5–t3 ([54.7%, 62.3%], confidence interval $p = 0.05$) and p5–t4 significant different from chance level (binomial test $p < 0.05$, [49.9%, 58.1%], confidence interval $p = 0.05$).

High-level accuracy during increased RRC was also obtained, equal to $85.7 \pm 3.8\%$, as shown in figure 2(b) ($n = 9$, see also supplementary figure 2(b) for confusion matrices). Also in this case we found a dependence on the electrode positioning within the same nerve. In all possible comparison (i.e. p3–s1 vs. p3–s2; p4–s3 vs. p4–s4; p5–t3 vs. p5–t4 and p6–t5 vs. p6–t6) we found significant differences between accuracies (figure 2(b), $p < 0.001$ Chi square test, Bonferroni correction).

Measurements during TVC yielded similar results compared to the other challenges, but with a stronger effect of the electrode positioning. In pig p2 that was implanted with TIME t2 (p2–t2), we achieved high accuracy level equal to 78.7% ([74.5%, 82.5%], confidence interval $p = 0.05$, see figure 2(c) and supplementary figure 2(c) for confusion matrices).

Moreover, the decoding accuracy during TVC was strongly dependent on the electrode positioning within the same nerve. In fact, in animals implanted with s1 and s4, i.e. p3–s1 and p4–s4, we obtained accuracy values near chance level for p3–s1 ([50.8%, 60.5%], confidence interval $p = 0.05$) and statistically not different from chance level for p4–s4 ($p > 0.05$, binomial test, [44.4%, 54.2%], confidence interval $p = 0.05$ see figure 2(c) and supplementary figure 2(c) for confusion matrices). In the same animals, but with different electrode positioning, we achieved a high level of accuracy of 85.6% for p3–s2 ([81.9%, 88.7%], confidence interval $p = 0.05$) and 73.4% for

p4–s3 ([68.9%, 77.6%], confidence interval $p = 0.05$, see figure 2(c) and supplementary figure 2(c) for confusion matrices).

3.3. Decoding the response to multiple functional challenges

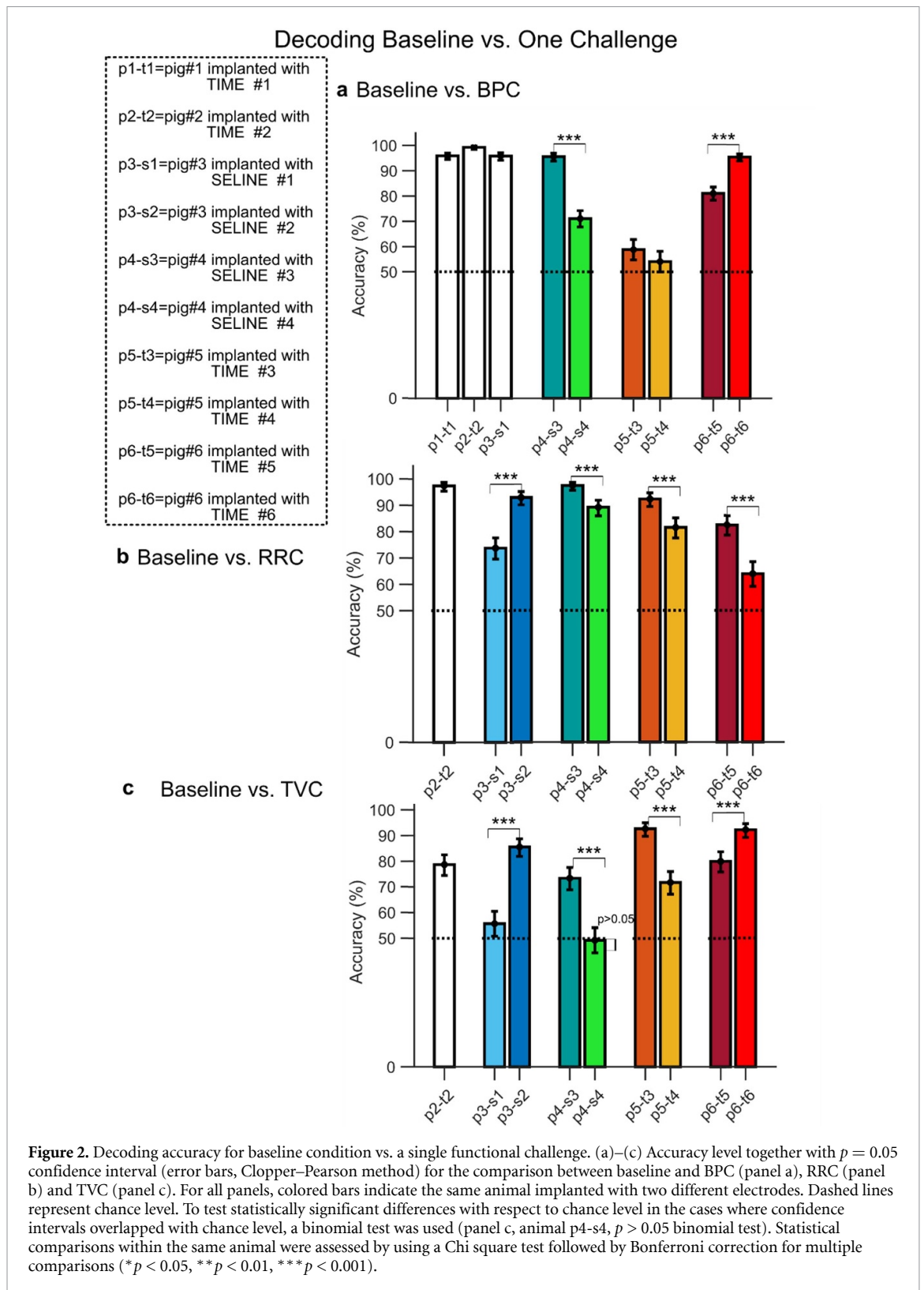
We increased the complexity of the decoding task by considering simultaneously within our dataset two functional challenges involving two different physiological systems, e.g. BPC + RRC or TVC, or in the same system, namely RRC + TVC.

The accuracy values for the BPC vs. RRC case were $74.4 \pm 5.1\%$ ($n = 8$), as shown in figure 3(a) and supplementary figure 3(a) for confusion matrices.

High accuracy values were achieved also for BPC vs TVC, with an overall mean over recordings $68.6 \pm 5.8\%$ ($n = 8$), as shown in figure 3(b) and supplementary figure 3(b) for confusion matrices. Dependency on electrode positioning within the same nerve was found in animals p4, p5, p6 for both BPC vs. RRC and BPC vs. TVC (figures 3(a) and (b), respectively, $p < 0.001$ Chi square test, Bonferroni correction).

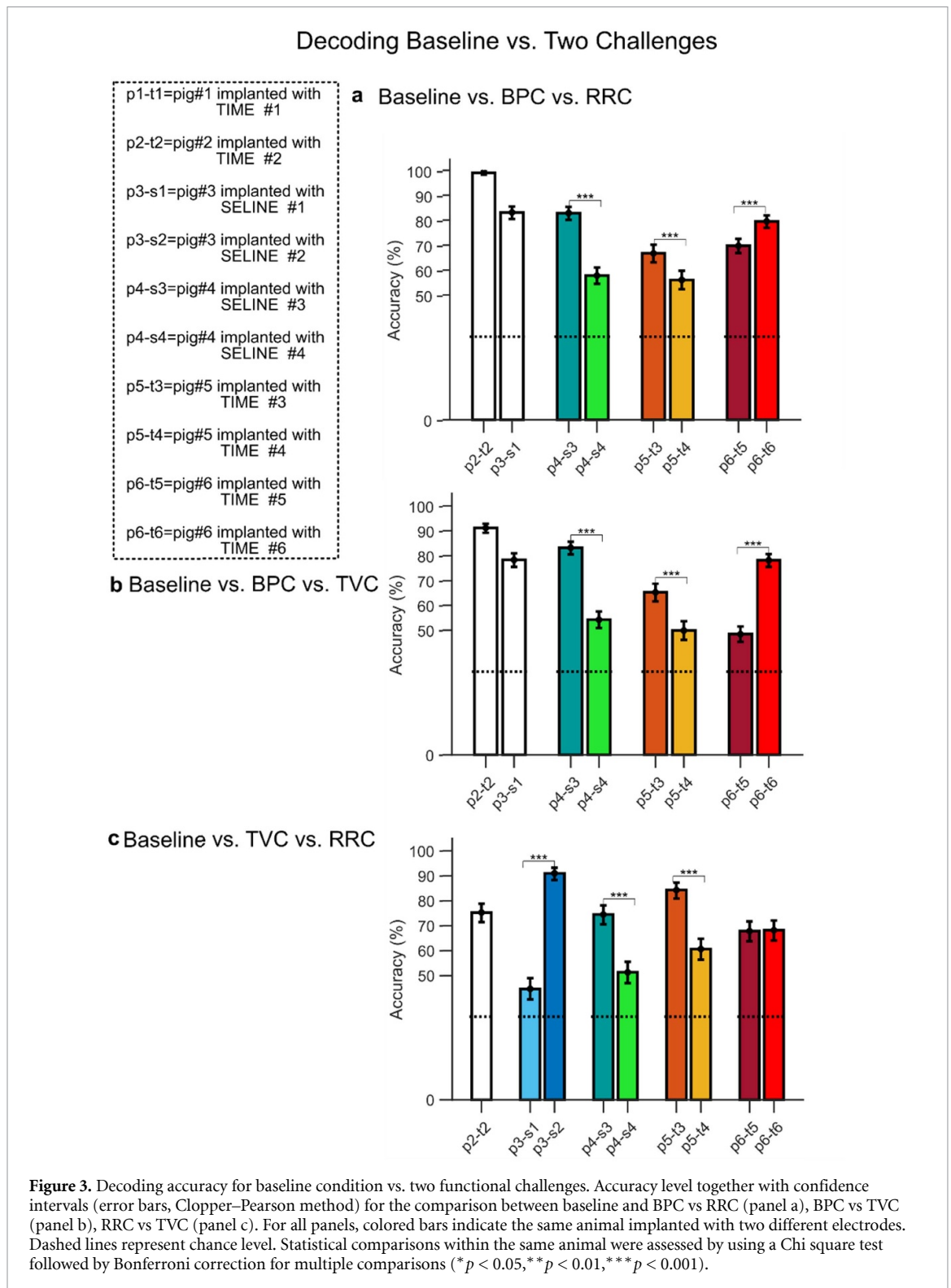
We were also able to reliably decode the two respiratory challenges RRC and TVC when simultaneously considered in our multiclass classification task. We found an overall accuracy mean over recordings equal to $68.6 \pm 4.9\%$ ($n = 9$), with a dependence on the electrode position in animals p3, p4, p5 but not in p6 where the electrodes t5 and t6 achieved a similar level of accuracy, 67.8% ([63.7%, 71.7%] confidence interval $p = 0.05$) and 68.2% ([64.1%, 72.1%] confidence interval $p = 0.05$), respectively, as shown in figure 3(c) ($p > 0.05$ Chi square test, Bonferroni correction) and supplementary figure 3(c) for confusion matrices.

Furthermore, we studied the most complex scenario of our decoding task in which all types of functional challenges (one cardiovascular and two respiratory) are considered simultaneously in our experimental dataset. As discussed above, also in this case we found that decoding performances depended on electrode positioning within the same nerve for animals p4, p5, p6 ($p < 0.001$ Chi square test, Bonferroni correction). The overall accuracy level is equal to $60.2 \pm 5\%$ ($n = 8$) where the highest accuracy among animals was obtained by TIME t2 implanted in p2, i.e. p2–t2, with a value equal to 84.8% ([82.6%, 86.8%] confidence interval $p = 0.05$) while the lowest accuracy value by TIME t5 implanted in p6, i.e. p6–t5 43.5% ([40.6%, 46.5%] confidence interval $p = 0.05$) (see figure 4(a)). We assessed also possible effects on the accuracy values due to the different side of VN (left or right) considered for the electrode implantation and the type of electrode (TIME or SELINE). To this aim, we employed a two-way ANOVA followed by Tukey–Kramer test



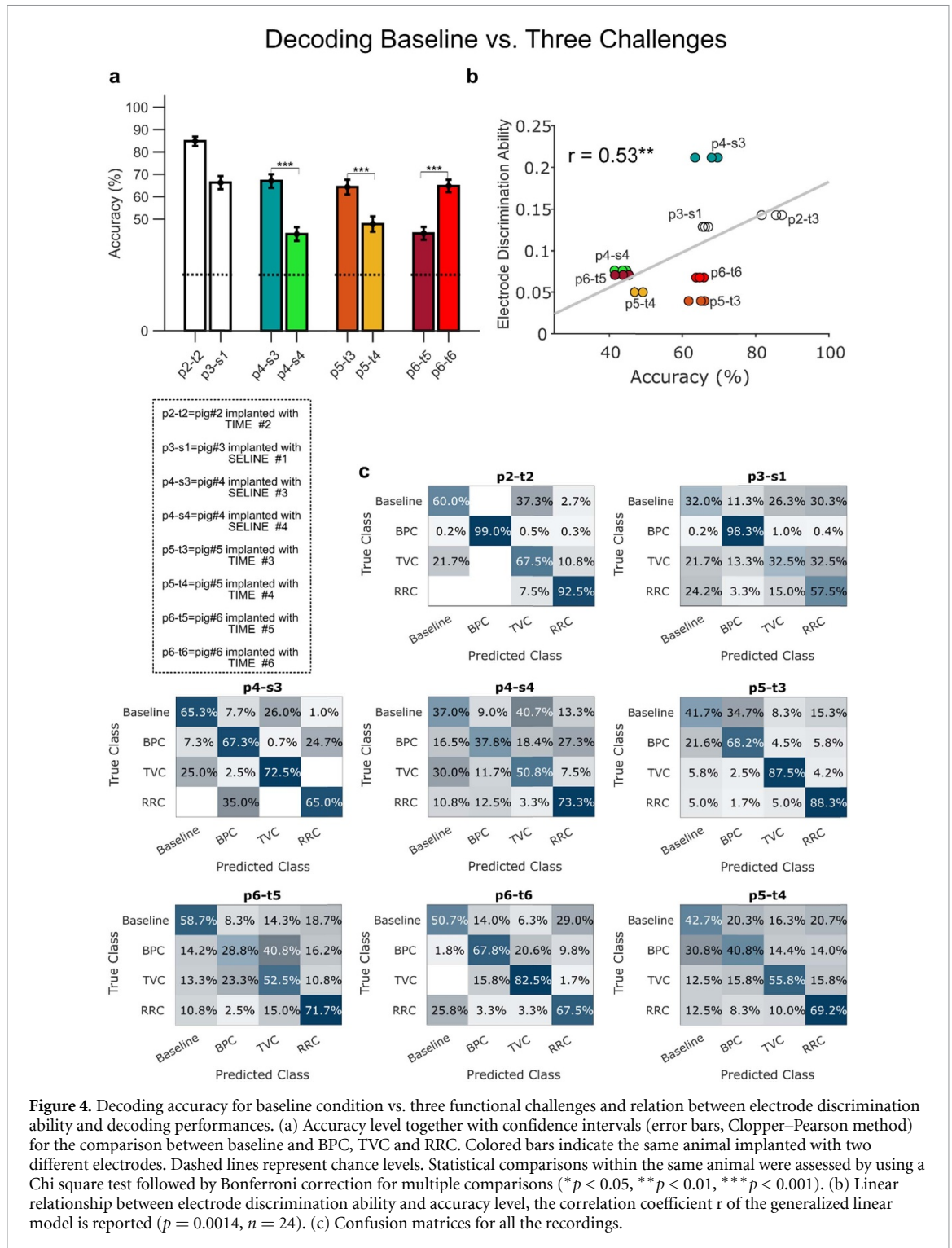
for multiple comparisons. We pooled together all the values of the accuracies ($n = 60$) obtained in the different decoding tasks and we found no significant effect of the type of electrodes, i.e. TIME vs. SELINE (mean \pm std: $74 \pm 16\%$ and $73 \pm 17\%$, respectively $p = 0.045$ see supplementary figure 1), while

a greater decoding accuracy was achieved from signals acquired from the left VN compared to right VN side (mean \pm std: $82 \pm 15\%$ and $70 \pm 15\%$, respectively $p = 0.045$ see supplementary figure 1). No interaction effect between side and electrode was found ($p = 0.11$).



Finally, to better understand why different accuracy values were obtained in our datasets, we sought a possible correlation between the electrode discrimination ability, i.e. the sensitivity of the recording sites to the specific challenges, and the decoding performance. Electrode discrimination ability (EDA) was assessed by calculating the percent activation of each recording site of the electrode with respect to the different functional challenges (see section 2

for details and supplementary figures 4 and 5 for a graphical example). In this way, the ensemble of channels activations yields a discrimination vector for each functional challenge. Intuitively, the greater the difference between those discrimination vectors representing different functional challenges, the more discriminative is the electrode (supplementary figures 5(b) and (c) for distance matrices). We thus employed a generalized linear model for accuracy (Acc) and



EDA treating the different folds (Kfold), over which we obtained the accuracy values, as a random effect, i.e. $\text{Acc} \sim \text{EDA} + (1|K\text{fold})$.

Our model consisted of $n = 24$ points, and we found a significant correlation $p = 0.0016$ with a correlation coefficient equal to $r = 0.81$ (see figure 4(b)).

3.4. A hybrid model framework to map the functional spatial organization of VN fascicles

The site-related sensitivity to specific functional challenges indicated a possible functional spatial

organization of VN fascicles, which we explored by combining the information obtained from histological analysis with simulations of electric potential field and discrimination properties of the electrodes.

The spatial relationship between VN fascicles and electrode active sites was determined by histological examination in one animal, p4. We reasonably assumed that the overall nerve morphology in terms of fascicular structure and organization is constant along the implant site, so we morphologically

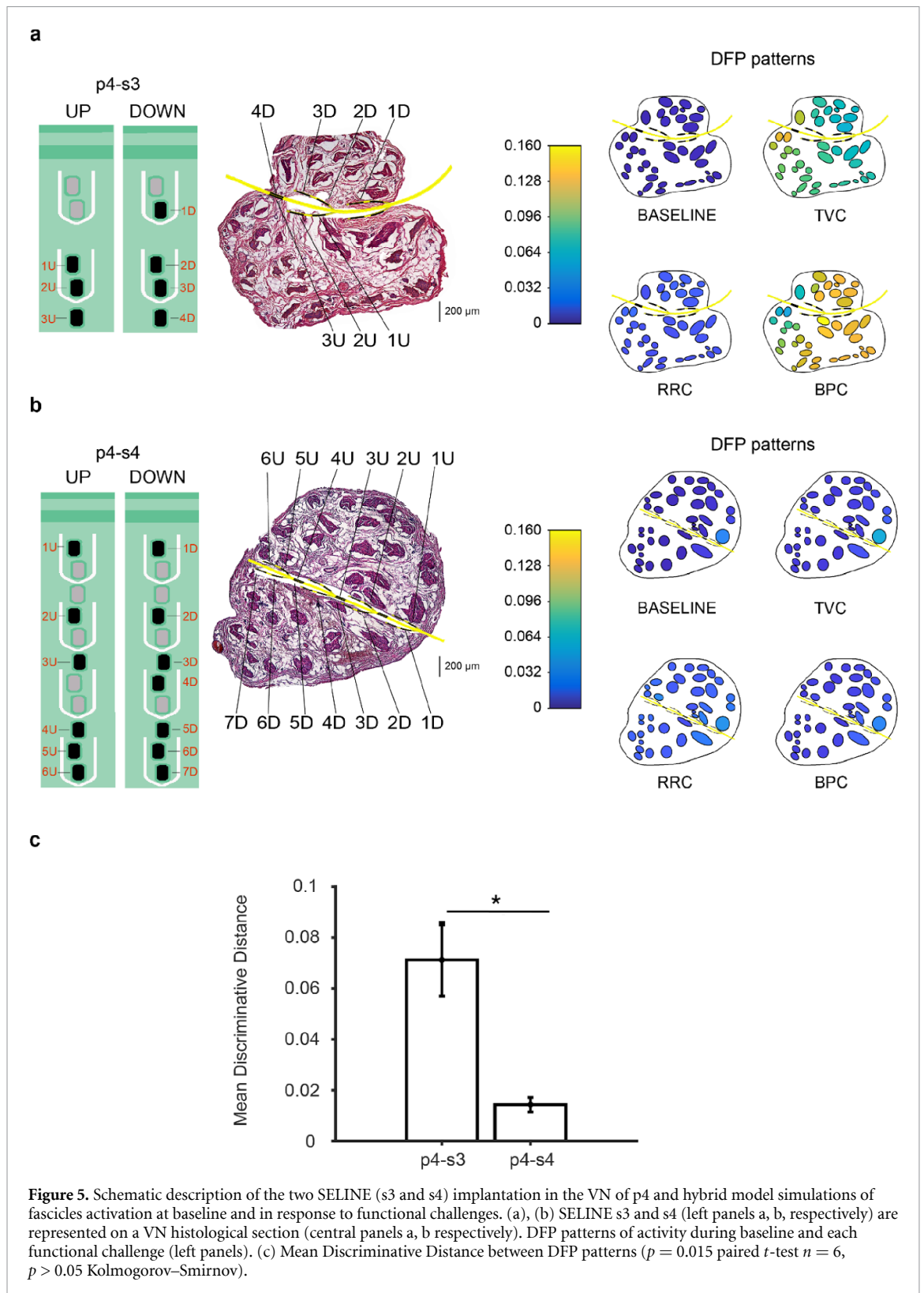


Figure 5. Schematic description of the two SELINE (s3 and s4) implantation in the VN of p4 and hybrid model simulations of fascicles activation at baseline and in response to functional challenges. (a), (b) SELINE s3 and s4 (left panels a, b, respectively) are represented on a VN histological section (central panels a, b respectively). DFP patterns of activity during baseline and each functional challenge (left panels). (c) Mean Discriminative Distance between DFP patterns ($p = 0.015$ paired t -test $n = 6$, $p > 0.05$ Kolmogorov–Smirnov).

modeled the SELINE active sites on the same 2D transverse section representation of the VN (figure 5 panels a, b, left and middle figures, for SELINES s3 and s4 implanted in p4, respectively).

Based on the histological analysis, we constructed a hybrid modeling framework [49–51] to understand the spatial distribution of electrical potential fields in the nerve sections of p4-s3 and p4-s4. In

supplementary figures 6 and 7 (panel b), isopotential electric field lines corresponding to each nerve section and three different recording sites are shown (p4-s3 and p4-s4, respectively). Using the Helmholtz reciprocity theorem [51], these potential values quantify the recording capability of a given active site favored by the specific position of a fascicle located inside the nerve [53]. Since we were interested in the

global electrical activity of fascicles, we employed a mean field approach by averaging the potential values within a given fascicle (supplementary figures 6 and 7 panel c, left) for nerve section p4–s3 and p4–s4, respectively.

To quantitatively characterize the association of a given fascicle with a specific functional challenge, we weighted the discrimination index of each active site with the mean field generated by that fascicle recorded from that active site. We then averaged data obtained from all recording sites and normalized the average to the total mean field, thus obtaining what we called DFP (DFP, see section 2 for details). In this way, we developed for the first time a quantitative measure characterizing how a fascicle is related to a given functional challenge. This measure could be considered the equivalent, for recording, of the selectivity index [21, 49] quantifying the stimulation ability on an electrode to elicit the activation of targeted fibers.

DFP patterns related to baseline condition and functional challenges were obtained for each nerve section p4–s3 and p4–s4, as shown in figures 5(a) and (b), right panels, respectively, and supplementary figures 6 and 7 panel c bottom, respectively. Interestingly, for both nerve sections p4–s3 and p4–s4, the baseline condition exhibited a balanced DFP pattern where each fascicle is activated in the same manner. On the contrary, DFP magnitude was higher and differences between DFP patterns within each nerve were more pronounced in p4–s3 than in p4–s4 as shown in figures 5(a) and (b), right panels, respectively, and supplementary figures 6 and 7 panel c bottom, respectively. We quantified them by calculating the root mean square level of the Euclidean distance among the DFP values of each fascicle for each possible comparison between functional challenges (mean discriminative distance). We found a statistically significant higher mean discriminative distance of the nerve in p4–s3 with respect to p4–s4 ($p = 0.015$ paired t -test, $n = 6$ all possible functional challenges combination). This was consistent with the higher effectiveness of decoding based on p4–s3 recordings.

4. Discussion

Bioelectronic medicine may lead to revolutionary treatments of an ample variety of diseases. However, therapeutic neuromodulatory interventions, especially those based on implantable systems, ought to be very precise, both spatially, activating specific nerve fibers, and temporally, i.e. operating in closed-loop to mimic the natural conditions. Therefore, it is necessary to utilize neural interfaces to selectively stimulate ANS nerves (spatial precision) and decode signals triggered by specific functional changes, so that the stimulation is activated only when necessary (temporal precision).

The present study provides the first evidence that signals recorded with intraneural electrodes in pig VN can be reliably used to detect functional changes in the cardiovascular and/or respiratory system.

We perturbed the homeostasis of one of both systems with functional challenges that were expected to enhance the activity of aortic baroreceptors and/or lung stretch receptors. Electrical signals departing from those receptors run along afferent fibers of the VN, carrying to the CNS information on blood pressure changes and lung inflation state [54]. Although induced by pharmacological and mechanical stimuli, in our study these hemodynamic and respiratory alterations mimicked very common pathophysiological conditions such as hypertension, tachypnea, and polypnea. Given the copresence of afferent and efferent fibers within the VN, our recordings inevitably captured signals traveling in the two directions, even though we can reasonably assume the major contribution was coming from afferent fibers as they outnumber the efferent.

Exploiting our previous experience with somatic nerves [31] and differently from previous studies [4, 22, 24, 25, 33, 34] that employed spike sorting methods [24, 25] or extracted neural profiles correlated with specific physiological variables [4, 22, 33, 34], we processed the whole high frequency components of our signals with an advanced machine learning approach, never applied to the VN before. This method proved successful in achieving high-level accuracy for decoding functional challenges. In such regard, the pig VN is ideal for the development of clinically relevant technologies. The fascicular organization of pig VN is the closest to the complexity of human VN intraneural morphology compared to other species commonly utilized in experimental research [35]. For instance, other studies have shown the possibility to decode different functional challenges in the murine VN [24, 25], which, unfortunately, contains less fibers and not subdivided in fascicles.

To the best of our knowledge, prior studies in pig VN [4, 22, 34] did not demonstrate the possibility to decode multiple functional challenges. While cuff [4, 22] and intraneural [34] electrodes in pigs proved effective in extrapolating neural markers of blood pressure and respiratory activity, no decoding analysis for the identification of mixed functional challenges was attempted. Moreover, the recordings with cuff electrodes [4, 22] were not obtained during the same experimental session.

In this study we exploited intraneural (TIMES and SELINES) electrodes, which are conceived to be transversally or obliquely inserted into the nerve, allowing spatially selective stimulation and recording from different fascicles innervating distinct peripheral targets [38–40, 55]. Our results show that the quality of decoding performances depends on the

electrode position. This could be due to the different functional role of fascicles adjacent to the recording sites and prompts the hypothesis of a specific spatial segregation of vagal fibers traversed by specific signals. Therefore, to map a possible spatial functional organization of VN fascicles, we employed a hybrid modeling framework based on histological analysis combined with electrode discrimination ability properties. We assumed that the discrimination of a given functional challenge in a given recording site was higher when the local fibers we activated by that specific stimulus and the local recording capability was high. Based on this assumption, we developed a novel quantitative measure called Discriminative Field Potential (DFP), obtaining distinct spatial configurations of discriminative patterns generated by fascicles during the various functional challenges. Moreover, placing a large number of active sites along the intraneural implant would augment the interfaces with fascicles, thus reducing the number of implanted electrodes [30, 56].

The present findings strongly suggest that multi-contact electrodes positioning is of crucial importance for bioelectronic applications in a complex nerve such as the VN. In our opinion, the development of an anatomical and electrophysiological *in silico* model of the VN would be extremely useful to guide electrodes implantation and positioning and to overcome the present limitations. Such model should incorporate the precise localization of organ-specific fascicles within the main vagal trunk, given the high rate of VN fasciculation occurring in pigs similar to other species like sheep and humans [57]. This marked fasciculation likely reflects an equivalent high spatial segregation of fibers innervating different peripheral sites and could be explored using techniques that allow 3D reconstructions like micro-CT [57]. Thus, anatomical reconstructions could be combined with techniques controlling the positioning of the active sites of intraneural electrodes [58] and the hybrid modeling framework developed here to find optimal spatial points for the decoding of physiological information. Ultimately, such approach would help in clarifying also the best VN side to realize VN decoding for specific VNS protocols.

5. Limitations and future directions

The present study was performed in an acute experimental preparation and it is known that anesthesia exerts important effects on neural activity and other physiological systems. For this reason, our next step will consist of validating the implantation of intraneural electrodes for VN chronic recordings in non-anesthetized animals. Another limitation relates to the mixed signals traveling along the intact VN: future studies will be specifically designed to precisely identify afferent versus efferent signals. Moreover,

we limited our analysis to isolated respiratory challenges, i.e. increase in TV and RR, as a preliminary approach to investigate different physiological mechanisms. Given the simultaneous occurrence of TV and RR variations in the real-life scenario, we plan to investigate this aspect in future studies for broader translational implications. Finally, an important step will be the implementation and validation of online signal analysis, necessary for closed-loop VNS protocols.

6. Conclusions

To summarize, we developed a decoding algorithm novel to VN studies that robustly achieved high accuracy levels in classifying different functional changes from VN signals. Interestingly, we found that electrodes positioning plays an important role on decoding performances. Finally, we suggested a functional topographical organization of VN fascicles by combining an anatomically validated hybrid neural model and a new index for the characterization of recording and decoding performance of neural interfaces. The present results represent an important step towards more precise neuromodulation protocols based on the knowledge of specific patterns of neural activations recordable in VN under physiological and pathological conditions. Advanced closed-loop and spatially selective VNS could improve the treatment of pathological conditions by selectively activating functionally specialized fiber fascicles, thus preventing the side-effects caused by the current technology.

The importance of understanding VN signals extends beyond VNS and closed-loop applications. Being the biggest peripheral crossroad of signals between the CNS and visceral organs, a sensitive and reliable technology for detection and decoding of VN activity could serve for the diagnosis of pathophysiological conditions otherwise difficult to detect. Deciphering the 'vagal language' will also help clarifying the mechanisms by which VNS exerts its curative effects and gaining deeper insights in the VN regulation of specific physiological processes.

Data availability statement

The data that support the findings of this study are available upon reasonable request from the authors.

Acknowledgments

This work was partly funded by the Bertarelli Foundation (www.fondation-bertarelli.org) and the EC H2020-FETPROACT-2018-01 NeuHeart (#824071).

Authors contributions

F V analyzed the data, developed the decoding algorithm, prepared the figures, and wrote the paper. M M O designed the study, performed the experiments and the histological analysis, prepared the figures, and wrote the paper. F D and A C performed the experiment and produced the electrodes. S R analyzed the data and wrote the manuscript. A M P and F B performed the experiments. M C analyzed the data. I S, K G and N G performed the experiments. A M, F A R and S M designed the study, supervised the experiments and reviewed the paper. All authors authorized the submission of the manuscript.

ORCID iDs

Fabio Vallone  <https://orcid.org/0000-0001-8911-9611>

Matteo Maria Ottaviani  <https://orcid.org/0000-0002-6354-3278>

Ivo Strauss  <https://orcid.org/0000-0003-0971-8783>

Alberto Mazzoni  <https://orcid.org/0000-0002-9632-1831>

References

- [1] Birmingham K, Gradinaru V, Anikeeva P, Grill W M, Pikov V, McLaughlin B, Pasricha P, Weber D, Ludwig K and Famm K 2014 Bioelectronic medicines: a research roadmap *Nat. Rev. Drug Discovery* **13** 399–400
- [2] Famm K, Litt B, Tracey K J, Boyden E S and Slaoui M 2013 A jump-start for electroceuticals *Nature* **496** 159–61
- [3] Cracchiolo M, Ottaviani M M, Panarese A, Strauss I, Vallone F, Mazzoni A and Micera S 2021 Bioelectronic medicine for the autonomic nervous system: clinical applications and perspectives *J. Neural Eng.* **18** 041002
- [4] Sevcencu C, Nielsen T N and Struijk J J 2017 A neural blood pressure marker for bioelectronic medicines for treatment of hypertension *Biosens. Bioelectron.* **98** 1–6
- [5] Johnson R L and Wilson C G 2018 A review of vagus nerve stimulation as a therapeutic intervention *J. Inflamm. Res.* **11** 203–13
- [6] George R et al 1995 A randomized controlled trial of chronic vagus nerve stimulation for treatment of medically intractable seizures *Neurology* **45** 224–30
- [7] Klein H U and De Ferrari G M 2010 Vagus nerve stimulation: a new approach to reduce heart failure *Cardiol. J.* **17** 638–43
- [8] Koopman F A et al 2016 Vagus nerve stimulation inhibits cytokine production and attenuates disease severity in rheumatoid arthritis *Proc. Natl Acad. Sci.* **113** 8284–9
- [9] Bonaz B et al 2016 Chronic vagus nerve stimulation in Crohn's disease: a 6 month follow-up pilot study *Neurogastroenterol. Motil.* **28** 948–53
- [10] Yuan H and Silberstein S D 2016 Vagus nerve and vagus nerve stimulation, a comprehensive review: part II *Headache: J. Head Face Pain* **56** 259–66
- [11] Tracey Kevin J 2005 The inflammatory reflex *Nature* **257** 122–5
- [12] Meyers E C, Solorzano B R, James J, Ganzer P D, Lai E S, Rennaker R L, Kilgard M P and Hays S A 2018 Vagus nerve stimulation enhances stable plasticity and generalization of stroke recovery *Stroke* **49** 710–7
- [13] Beekwilder J P and Beems T 2010 Overview of the clinical applications of vagus nerve stimulation *J. Clin. Neurophysiol.* **27** 130–8
- [14] Citi L, Carpaneto J, Yoshida K, Hoffmann K P, Koch K P, Dario P and Micera S 2008 On the use of wavelet denoising and spike sorting techniques to process electroneurographic signals recorded using intraneural electrodes *J. Neurosci. Methods* **172** 294–302
- [15] Ganzer P D and Sharma G 2019 Opportunities and challenges for developing closed-loop bioelectronic medicines *Neural Regen. Res.* **14** 46–50
- [16] Zanos S 2019 Closed-loop neuromodulation in physiological and translational research *Cold Spring Harbor Perspect. Med.* **9** a034314
- [17] Micera S, Carpaneto J and Raspopovic S 2010 Control of hand prostheses using peripheral information *IEEE Rev. Biomed. Eng.* **3** 48–68
- [18] Sun F T and Morrell M J 2014 Closed-loop neurostimulation: the clinical experience *Neurotherapeutics* **11** 553–63
- [19] Bouton C 2015 Neural decoding and applications in bioelectronic medicine *Bioelectron. Med.* **2** 20–4
- [20] Xue N, Martinez I D, Sun J, Cheng Y and Liu C 2018 Flexible multichannel vagus nerve electrode for stimulation and recording for heart failure treatment *Biosens. Bioelectron.* **112** 114–9
- [21] Raspopovic S, Capogrosso M, Badia J, Navarro X and Micera S 2012 Experimental validation of a hybrid computational model for selective stimulation using transverse intrafascicular multichannel electrodes *IEEE Trans. Neural Syst. Rehabil. Eng.* **20** 395–404
- [22] Sevcencu C, Nielsen T N, Kjærgaard B and Struijk J J 2017 A respiratory marker derived from left vagus nerve signals recorded with implantable cuff electrodes *Neuromodulation* **21** 269–75
- [23] Metcalfe B W, Nielsen T N, Donaldson N D N, Hunter A J and Taylor J T 2018 First demonstration of velocity selective recording from the pig vagus using a nerve cuff shows respiration afferents *Biomed. Eng. Lett.* **8** 127–36
- [24] Zanos T P, Silverman H A, Levy T, Tsaava T, Battinelli E, Lorraine P W, Ashe J M, Chavan S S, Tracey K J and Bouton C E 2018 Identification of cytokine-specific sensory neural signals by decoding murine vagus nerve activity *Proc. Natl Acad. Sci. USA* **115** E4843–52
- [25] Battinelli E, Levy T, Tsaava T, Bouton C E, Tracey K J, Chavan S S and Zanos T P 2018 Identification of hypoglycemia-specific neural signals by decoding murine vagus nerve *Bioelectron. Med.* **115** E4843–52
- [26] Cracchiolo M, Sacramento J F, Mazzoni A, Panarese A, Carpaneto J, Conde S V and Micera S 2019 Decoding neural metabolic markers from the carotid sinus nerve in a type 2 diabetes model *IEEE Trans. Neural Syst. Rehabil. Eng.* **27** 2034–43
- [27] Navarro X, Krueger T B, Lago N, Micera S, Stieglitz T and Dario P 2005 A critical review of interfaces with the peripheral nervous system for the control of neuroprostheses and hybrid bionic systems *J. Peripher. Nerv. Syst.* **10** 229–58
- [28] Raspopovic S, Carpaneto J, Udina E, Navarro X and Micera S 2010 On the identification of sensory information from mixed nerves by using single-channel cuff electrodes *J. Neuroeng. Rehabil.* **7** 1–15
- [29] Rozman J and Ribarič S 2007 Selective recording of electroneurograms from the left vagus nerve of a dog during stimulation of cardiovascular or respiratory systems *Chin. J. Physiol.* **50** 240–50
- [30] Micera S et al 2011 Decoding of grasping information from neural signals recorded using peripheral intrafascicular interfaces *J. Neuroeng. Rehabil.* **8** 53
- [31] Rossini P M et al 2010 Double nerve intraneural interface implant on a human amputee for robotic hand control *Clin. Neurophysiol.* **121** 777–83

- [32] Cracchiolo M, Valle G, Petrini F M, Strauss I, Granata G, Stieglitz T, Rossini P M, Raspopovic S, Mazzoni A and Micera S 2020 Decoding of grasping tasks from intraneural recordings in trans-radial amputee *J. Neural Eng.* **17** 026034
- [33] Ottaviani M M, Wright L, Dawood T and Macefield V G 2020 *In vivo* recordings from the human vagus nerve using ultrasound-guided microneurography *J. Physiol.* **598** 3569–76
- [34] Sevcencu C, Nielsen T N and Struijk J J 2018 An intraneural electrode for bioelectronic medicines for treatment of hypertension *Neuromodulation* **21** 777–86
- [35] Settell M L et al 2020 Functional vagotomy in the cervical vagus nerve of the domestic pig: implications for the study of vagus nerve stimulation *J. Neural Eng.* **17** 26022
- [36] Gabisonia K et al 2019 MicroRNA therapy stimulates uncontrolled cardiac repair after myocardial infarction in pigs *Nature* **569** 418–22
- [37] Labinskyy V, Bellomo M, Chandler M P, Young M E, Lionetti V, Qanud K, Bigazzi F, Sampietro T, Stanley W C and Recchia F A 2007 Chronic activation of peroxisome proliferator-activated receptor- α with fenofibrate prevents alterations in cardiac metabolic phenotype without changing the onset of decompensation in pacing-induced heart failure *J. Pharmacol. Exp. Ther.* **321** 165–71
- [38] Boretius T, Badia J, Pascual-Font A, Schuettler M, Navarro X, Yoshida K and Stieglitz T 2010 A transverse intrafascicular multichannel electrode (TIME) to interface with the peripheral nerve *Biosens. Bioelectron.* **26** 62–9
- [39] Badia J, Raspopovic S, Carpaneto J, Micera S and Navarro X 2016 Spatial and functional selectivity of peripheral nerve signal recording with the transversal intrafascicular multichannel electrode (TIME) *IEEE Trans. Neural Syst. Rehabil. Eng.* **24** 20–7
- [40] Cutrone A, Del V J, Santos D, Badia J, Filippeschi C, Micera S, Navarro X and Bossi S 2015 A three-dimensional self-opening intraneural peripheral interface (SELINe) *J. Neural Eng.* **12** 16016
- [41] Recchia F A, Osorio J C, Chandler M P, Xu X, Panchal A R, Lopaschuk G D, Hintze T H and Stanley W C 2002 Reduced synthesis of NO causes marked alterations in myocardial substrate metabolism in conscious dogs *Am. J. Physiol.* **282** 197–206
- [42] Mallat S G 1989 A theory for multiresolution signal decomposition: the wavelet representation *IEEE Trans. Pattern Anal. Mach. Intell.* **11** 674–93
- [43] Mallat S 2009 *A Wavelet Tour of Signal Processing* (Amsterdam: Elsevier Inc.)
- [44] Raspopovic S, Cimolato A, Panarese A, Vallone F, Del Valle J, Micera S and Navarro X 2020 Neural signal recording and processing in somatic neuroprosthetic applications. A review *J. Neurosci. Methods* **337** 108653
- [45] Bakshi B R 1998 Multiscale PCA with application to multivariate statistical process monitoring *AIChE J.* **44** 1596–610
- [46] Breiman L, Friedman J H, Jerome H, Olshen R A and Stone C J 1984 *Classification and Regression Trees* (Boca Raton, Florida: Chapman and Hall/CRC)
- [47] Hastie T, Tibshirani R and Friedman J 2009 *The Elements of Statistical Learning the Elements of Statistical Learning Data Mining, Inference, and Prediction* 2nd edn (New York: Springer-Verlag)
- [48] Galar M, Fernandez A, Barrenechea E, Bustince H and Herrera F 2012 A review on ensembles for the class imbalance problem: bagging-, boosting-, and hybrid-based approaches *IEEE Trans. Syst. Man Cybern. C* **42** 463–84
- [49] Raspopovic S, Capogrosso M and Micera S 2011 A computational model for the stimulation of rat sciatic nerve using a transverse intrafascicular multichannel electrode *IEEE Trans. Neural Syst. Rehabil. Eng.* **19** 333–44
- [50] Raspopovic S, Petrini F M, Zelechowski M and Valle G 2017 Framework for the development of neuroprostheses: from basic understanding by sciatic and median nerves models to bionic legs and hands *Proc. IEEE* **105** 34–49
- [51] Romeni S, Valle G, Mazzoni A and Micera S 2020 Tutorial: a computational framework for the design and optimization of peripheral neural interfaces *Nat. Protoc.* **15** 3129–53
- [52] Grinberg Y, Schiefer M A, Tyler D J and Gustafson K J 2008 Fascicular perineurium thickness, size, and position affect model predictions of neural excitation *IEEE Trans. Neural Syst. Rehabil. Eng.* **16** 572–81
- [53] Jehenne B, Raspopovic S, Capogrosso M, Arleo A and Micera S 2015 Recording properties of an electrode implanted in the peripheral nervous system: a human computational model *Int. IEEE/EMBS Conf. Neural Eng. NER (July 2015)* pp 482–5
- [54] Paintal A S 1973 Vagal sensory receptors and their reflex effects *Physiol. Rev.* **53** 159–227
- [55] Gaillet V, Cutrone A, Artoni F, Vagni P, Mega Pratiwi A, Romero S A, Di Paola D L, Micera S and Ghezzi D 2019 Spatially selective activation of the visual cortex via intraneural stimulation of the optic nerve *Nat. Biomed. Eng.* **4** 181–94
- [56] Verplancke R et al 2020 Development of an active high-density transverse intrafascicular micro-electrode probe *J. Micromech. Microeng.* **30** 015010
- [57] Thompson N, Ravagli E, Mastitskaya S, Iacoviello F, Aristovich K, Perkins J, Shearing P R and Holder D 2020 MicroCT optimisation for imaging fascicular anatomy in peripheral nerves *J. Neurosci. Methods* **338** 108652
- [58] Bossi S, Micera S, Menciassi A, Beccai L, Hoffmann K P, Koch K P and Dario P 2006 On the actuation of thin film longitudinal intrafascicular electrodes *Proc. First IEEE/RAS-EMBS Int. Conf. Biomed. Robot. Biomechatronics, 2006, BioRob 2006* **0** 383–8